Multiscale photoacoustic tomography using reversibly switchable bacterial phytochrome as a near-infrared photochromic probe

Junjie Yao[1,6], Andrii A Kaberniuk[2,3,6], Lei Li[1,6], Daria M Shcherbakova[2,3], Ruiying Zhang[1], Lidai Wang[1,5], Guo Li[1], Vladislav V Verkhusha[2–4] & Lihong V Wang[1]

Photoacoustic tomography (PAT) of genetically encoded probes allows for imaging of targeted biological processes deep in tissues with high spatial resolution; however, high background signals from blood can limit the achievable detection sensitivity. Here we describe a reversibly switchable nonfluorescent bacterial phytochrome for use in multiscale photoacoustic imaging, BphP1, with the most red-shifted absorption among genetically encoded probes. BphP1 binds a heme-derived biliverdin chromophore and is reversibly photoconvertible between red and near-infrared light-absorption states. We combined single-wavelength PAT with efficient BphP1 photoswitching, which enabled differential imaging with substantially decreased background signals, enhanced detection sensitivity, increased penetration depth and improved spatial resolution. We monitored tumor growth and metastasis with ~100-μm resolution at depths approaching 10 mm using photoacoustic computed tomography, and we imaged individual cancer cells with a suboptical-diffraction resolution of ~140 nm using photoacoustic microscopy. This technology is promising for biomedical studies at several scales.

Optical imaging has provided valuable information for biomedical studies[1,2]. However, strong light scattering in tissue leads to a substantial tradeoff between spatial resolution and penetration depth[3]. PAT overcomes the depth and resolution limitations of pure optical imaging by acoustically detecting optical absorption contrast (Online Methods)[4]. The weak ultrasonic scattering in soft tissue provides PAT with highly scalable spatial resolution and penetration[5–11]. PAT is inherently suited for molecular imaging using genetically encoded optical probes[12–15] (either fluorescent or not). Genetically encoded optical probes with the following characteristics are highly desirable in PAT: (i) spectral properties that allow light penetration to deep tissues and robust unmixing from other endogenous biomolecules, (ii) light-sensing chromophores that are naturally present in tissues, and (iii) orthogonality to mammalian cell metabolism. Bacterial phytochromes (BphPs) are among the very few light-sensing proteins that meet these criteria.

BphPs are photoreceptors sensitive to light in the range of 600–800 nm (ref. 16), which falls into the optical window in tissue[17]. BphPs consist of a photosensory core module and an output effector domain (**Supplementary Fig. 1a**). The spectral properties of BphPs are defined by a covalently attached chromophore, biliverdin IXα (BV)[18] (**Supplementary Fig. 1b**). Inside a chromophore-binding pocket, photoisomerization of BV leads to two conformational states, Pfr and Pr, resulting in a shift in absorption spectrum[19] (**Supplementary Fig. 1c**). For unbound BV molecules in cells, photoisomerization occurs but does not change the absorption spectrum (**Supplementary Fig. 1d**).
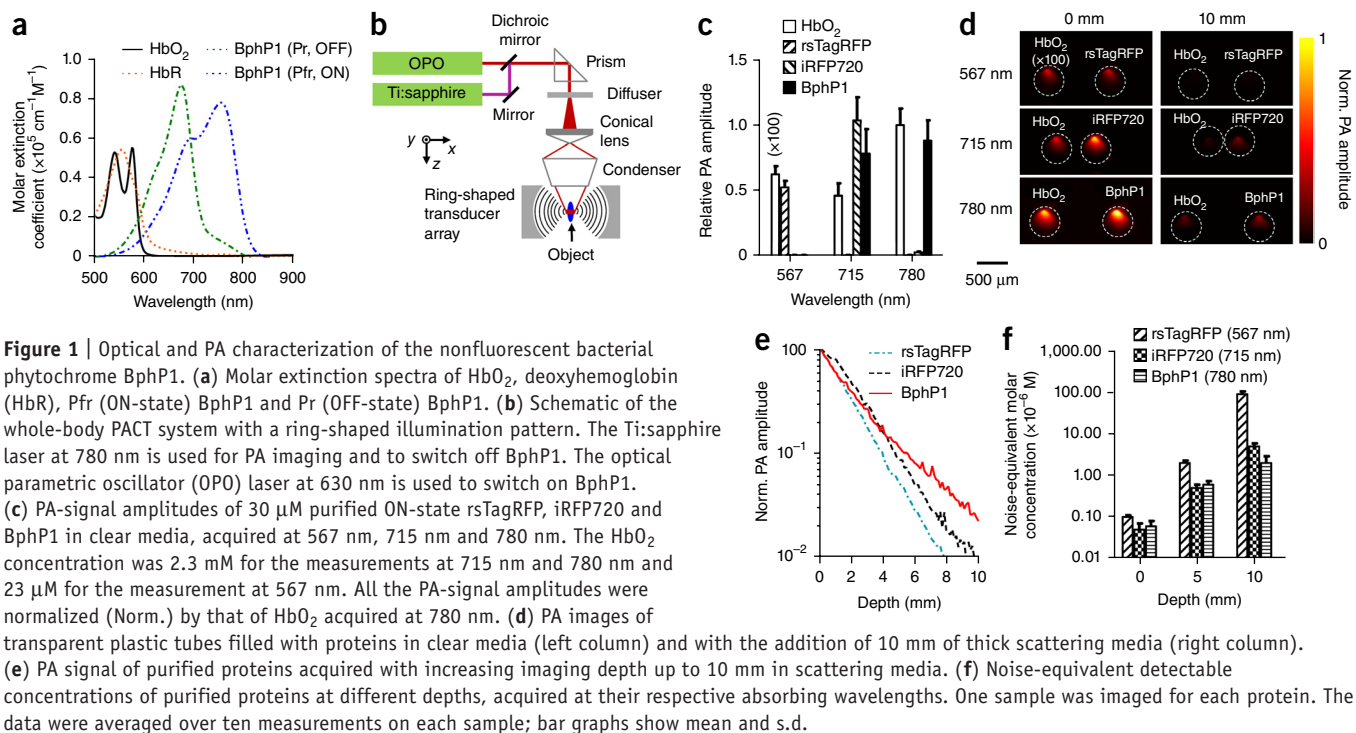
Here we report a novel imaging approach that combines PAT with an *Rp*BphP1 phytochrome from the bacterium *Rhodopseudomonas palustris* (referred to as BphP1). We investigated two embodiments of PAT—photoacoustic computed tomography (PACT) and photoacoustic microscopy (PAM)[4]—at different scales of penetration depth and spatial resolution. Our experiments capitalized on BphP1's reversible switching, and the results show that this imaging approach dramatically enhanced the detection sensitivity of PACT at large depths. We demonstrated the high detection sensitivity *in vivo* by imaging the growth of BphP1-expressing tumors and monitoring the tumor metastases over prolonged periods of time. We extended this imaging approach to super-resolution PAM and achieved substantially finer spatial resolutions and higher image contrast than in conventional PAM.

RESULTS
Comparison of BphP1 with available genetically encoded probes
BphP1 has a natural photochromic behavior: it adopts a Pfr state as the ground state, and it undergoes Pfr→Pr photoconversion upon 730–790-nm light illumination and Pr→Pfr photoconversion upon 630–690-nm light illumination. We assigned the Pfr state

[1]Department of Biomedical Engineering, Washington University in St. Louis, St. Louis, Missouri, USA. [2]Department of Anatomy and Structural Biology, Albert Einstein College of Medicine, Bronx, New York, USA. [3]Gruss-Lipper Biophotonics Center, Albert Einstein College of Medicine, Bronx, New York, USA. [4]Department of Biochemistry and Developmental Biology, Faculty of Medicine, University of Helsinki, Helsinki, Finland. [5]Present address: Department of Mechanical and Biomedical Engineering, City University of Hong Kong, Kowloon, Hong Kong, China. [6]These authors contributed equally to this work. Correspondence should be addressed to V.V.V. (vladislav.verkhusha@einstein.yu.edu) or L.V.W. (lhwang@wustl.edu).

Figure 1 | Optical and PA characterization of the nonfluorescent bacterial phytochrome BphP1. (**a**) Molar extinction spectra of HbO$_2$, deoxyhemoglobin (HbR), Pfr (ON-state) BphP1 and Pr (OFF-state) BphP1. (**b**) Schematic of the whole-body PACT system with a ring-shaped illumination pattern. The Ti:sapphire laser at 780 nm is used for PA imaging and to switch off BphP1. The optical parametric oscillator (OPO) laser at 630 nm is used to switch on BphP1. (**c**) PA-signal amplitudes of 30 μM purified ON-state rsTagRFP, iRFP720 and BphP1 in clear media, acquired at 567 nm, 715 nm and 780 nm. The HbO$_2$ concentration was 2.3 mM for the measurements at 715 nm and 780 nm and 23 μM for the measurement at 567 nm. All the PA-signal amplitudes were normalized (Norm.) by that of HbO$_2$ acquired at 780 nm. (**d**) PA images of transparent plastic tubes filled with proteins in clear media (left column) and with the addition of 10 mm of thick scattering media (right column). (**e**) PA signal of purified proteins acquired with increasing imaging depth up to 10 mm in scattering media. (**f**) Noise-equivalent detectable concentrations of purified proteins at different depths, acquired at their respective absorbing wavelengths. One sample was imaged for each protein. The data were averaged over ten measurements on each sample; bar graphs show mean and s.d.

of BphP1 as the ON state and the Pr state as the OFF state, and we used 780-nm light for Pfr→Pr photoconversion and 630-nm light for Pr→Pfr photoconversion. The molar extinction coefficients of BphP1 in the ON state at 780 nm and in the OFF state at 630 nm were, respectively, ~70-fold and ~40-fold higher than that of oxyhemoglobin (HbO$_2$) (**Fig. 1a** and **Supplementary Table 1**). We compared BphP1 with the most red-shifted near-infrared (NIR) fluorescent protein (FP) reported so far, iRFP720, which was engineered from another BphP[20]. Although the peak absorption of iRFP720 at 705 nm is comparable to that of the ON-state BphP1 at 780 nm, iRFP720 is not photoswitchable (**Supplementary Fig. 2a** and **Supplementary Table 1**). We also compared BphP1 with the most red-shifted photoswitchable FP reported so far, rsTagRFP, which can be photoswitched by altering light illumination between 440 nm and 570 nm (refs. 21,22). BphP1 was clearly more advantageous than rsTagRFP for deep-tissue imaging because of its twofold higher extinction coefficient and ~200-nm red-shifted absorption (**Supplementary Fig. 2a** and **Supplementary Table 1**).

We upgraded our whole-body mouse PACT system to use BphP1 (ref. 23) (**Fig. 1b**, Online Methods and **Supplementary Video 1**). To compare the performance of iRFP720, rsTagRFP and BphP1, we selected three wavelengths—567 nm, 715 nm and 780 nm—on the basis of the absorption spectra of the proteins and the power spectra of the lasers. Plastic tubes with purified proteins (~30 μM) were first immersed in water for photoacoustic (PA) imaging (**Supplementary Fig. 2b**). The laser fluence (8 mJ cm^{-2}) at all three wavelengths was within the American National Standards Institute safety limit for laser exposure (20 mJ cm^{-2} at 567 nm; 40 mJ cm^{-2} at 715 nm and 780 nm). The results clearly suggest the superior PA-signal generation of ON-state BphP1 at 780 nm (**Fig. 1c**). Purified proteins were then embedded at different depths in scattering media[24] (1% intralipid and 10% gelatin in distilled water; reduced scattering coefficient of ~10 cm^{-1}) (**Fig. 1d**). The PA-signal amplitude at a depth of 10 mm decreased ~32-fold

for BphP1 at 780 nm, ~101-fold for iRFP720 at 715 nm and ~320-fold for rsTagRFP at 567 nm (**Fig. 1e** and **Supplementary Table 1**). The noise-equivalent detection concentration was 2.0 ± 0.9 μM for BphP1 at 780 nm at 10-mm depth (**Fig. 1f**).

Characterization of reversible photoswitching of BphP1

Reversible photoswitching is an important feature of BphP1 for PAT, as it enables differential imaging with sensitivity that is, in principle, limited only by the noise level[14,25,26]. The photoswitching of BphP1 consists of a *cis-trans* photoisomerization of the D-ring of the biliverdin chromophore around its C15=C16 double bond[27] (**Supplementary Fig. 1c**). Because the D-ring can rotate in only one direction, the intermediate conformations are different during *cis*→*trans* and *trans*→*cis* photoswitching, which results in different Pr→Pfr and Pfr→Pr photoswitching rates (**Fig. 2a**). Once BphP1 is photoswitched to the OFF state, it naturally relaxes back to the ON state with a half-life of ~210 s. Multiple switching cycles did not cause photobleaching of BphP1. Because BphP1 photoswitching is a one-photon process, the photoswitching rate is approximately proportional to the switching light intensity (**Fig. 2b**), similar to what has been observed in photoswitchable FPs[21,25,28].

We evaluated photoswitching of BphP1 in scattering media at different depths using PACT (termed reversibly switchable (RS)-PACT). Here we define the switching ratio as the ratio of the measured PA-signal amplitude in the ON state of BphP1 to that in the OFF state. Each switching cycle consisted of 16 s of 780-nm light illumination for both PA imaging and switching off of BphP1, followed by 16 s of 630-nm light illumination only for switching on the protein (**Fig. 2c**). During the first 3.2 s of a switching cycle, a 630-nm laser pulse was fired 72 μs after each 780-nm laser pulse to maintain the protein population in the ON state. We used the PA images acquired during the first and last 3.2 s of the 780-nm light illumination as the ON-state and OFF-state images, respectively. Pixelwise subtraction of the OFF image from the ON

image generated a differential image. The switching wavelengths for other proteins were adjusted accordingly. Unless otherwise stated, a global threshold was applied to differential images, with a threshold level set at three times the noise level, estimated as the s.d. of the background signal outside the imaged region.

HbO_2 and iRFP720 could not be photoswitched (**Fig. 2d** and **Supplementary Fig. 3**). rsTagRFP had a switching ratio of 8.5 ± 0.3 in clear media, but it essentially could not be photoswitched at depths beyond 3 mm, because of the strong light attenuation at 440 nm and 567 nm (**Supplementary Table 1**). The photoswitching capability of BphP1 at 630 nm and 780 nm, however, was maintained at increased depths, and the switching ratio decreased only from 4.3 ± 0.2 in clear media to 2.8 ± 0.2 at 10-mm depth (**Fig. 2d** and **Supplementary Table 1**). We imaged the three proteins at 10-mm depth with oxygenated whole bovine blood as a reference (**Fig. 1d**). We quantified the contrast (difference between proteins and blood)-to-noise ratio (CNR) of the ON state and differential PA images (**Fig. 2e** and **Supplementary Table 1**). The differential PA image of BphP1 had ~21-fold enhancement in CNR relative to the ON-state image (**Fig. 2f**). The red and NIR switching of BphP1 are clearly advantageous for deep PA imaging.

RS-PACT of BphP1 in mammalian cells and *in vivo*

We used U87 human glioblastoma cells to stably express BphP1 (Online Methods). Because BphP1 is nonfluorescent, we used a plasmid containing an internal ribosome entry site between BphP1 and EGFP. Both genes were translated from a single bicistronic mRNA (**Supplementary Fig. 4a**). We used the coexpressed EGFP to select stable BphP1-expressing cells, study the cytotoxicity of BphP1 and validate the PA imaging.

We imaged BphP1-expressing U87 cells embedded in scattering media (1% intralipid, 10% gelatin and 2% oxygenated bovine blood in distilled water; absorption coefficient of $0.1\ cm^{-1}$; reduced scattering coefficient of $\sim 10\ cm^{-1}$) at 10-mm depth using RS-PACT. The PA images acquired before and after the photoswitching both had strong background signals from blood, resulting in poor image contrast of the U87 cells (**Supplementary Fig. 4b**). By contrast, the differential image, averaged over 20 switching cycles, was largely devoid of nonswitchable background signals and showed a 50-fold enhancement in CNR (**Supplementary Fig. 4c**). Multiple switching cycles did not cause photobleaching of the cells (**Supplementary Fig. 4d**). We observed the noise-equivalent detection sensitivity of ~20 cells by using differential PA imaging (**Fig. 3a**).

We compared the new single-wavelength differential method with the traditional two-wavelength spectral unmixing method (**Supplementary Fig. 5**). The two-wavelength method, based on least-squares fitting, had low accuracy in identifying the cells, largely due to the unknown optical fluence inside the scattering phantom. By contrast, the single-wavelength differential method was able to extract the BphP1 signals with greater accuracy, achieving a 34-fold enhancement in CNR.

We then tested whether BphP1 has low cytotoxicity, similar to FPs engineered from various natural BphPs[20,25]. First, we compared the cell viability of the BphP1-expressing U87 cells with that of the wild-type U87 cells by means of annexin V staining. We observed no difference between the two types of cells (**Supplementary Fig. 6a**). Second, we monitored the BphP1-expressing U87 preclonal cell culture for many generations. We did not observe a decrease in expression levels of BphP1 (measured by PAM) or EGFP (measured by fluorescence
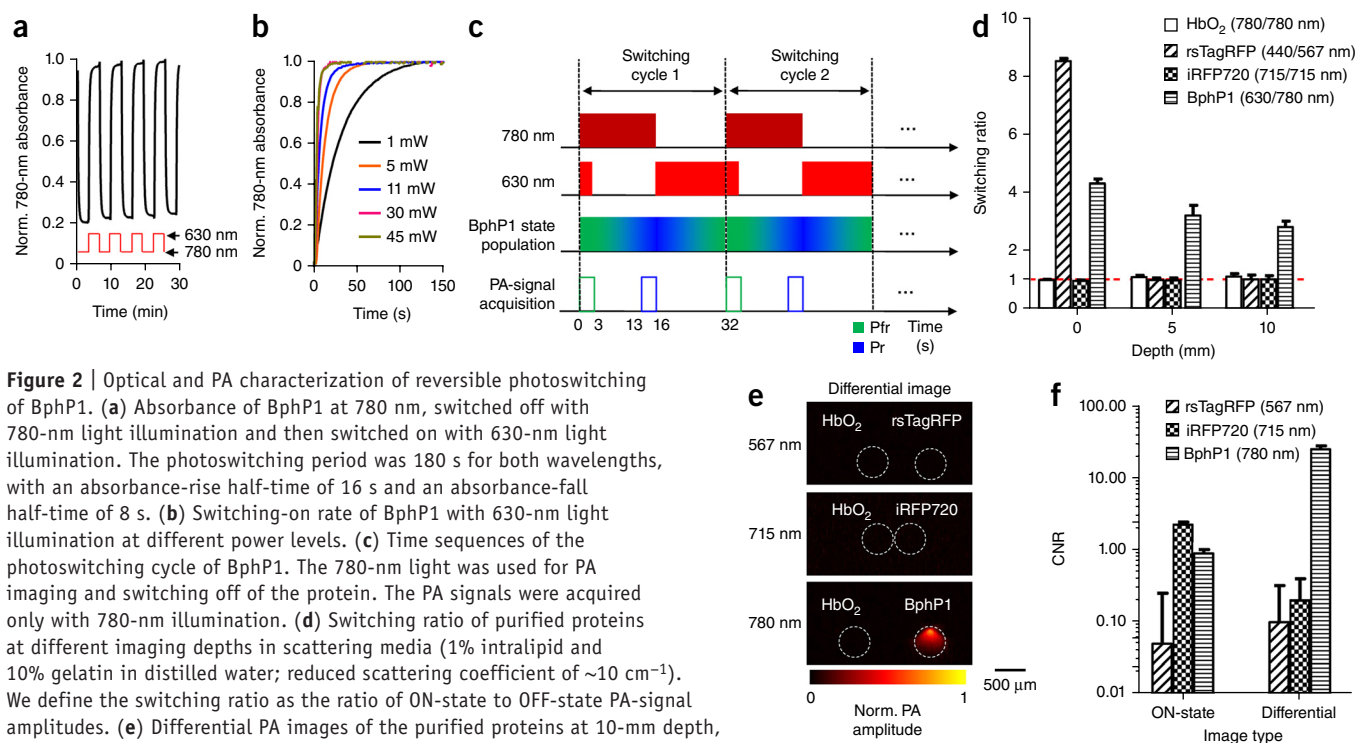
Figure 2 | Optical and PA characterization of reversible photoswitching of BphP1. (**a**) Absorbance of BphP1 at 780 nm, switched off with 780-nm light illumination and then switched on with 630-nm light illumination. The photoswitching period was 180 s for both wavelengths, with an absorbance-rise half-time of 16 s and an absorbance-fall half-time of 8 s. (**b**) Switching-on rate of BphP1 with 630-nm light illumination at different power levels. (**c**) Time sequences of the photoswitching cycle of BphP1. The 780-nm light was used for PA imaging and switching off of the protein. The PA signals were acquired only with 780-nm illumination. (**d**) Switching ratio of purified proteins at different imaging depths in scattering media (1% intralipid and 10% gelatin in distilled water; reduced scattering coefficient of $\sim 10\ cm^{-1}$). We define the switching ratio as the ratio of ON-state to OFF-state PA-signal amplitudes. (**e**) Differential PA images of the purified proteins at 10-mm depth, acquired at their respective wavelengths. HbO_2 was imaged with each protein to provide a reference. (**f**) Comparison of CNRs quantified from the ON-state images and the differential images. One sample was imaged for each protein. The data were averaged over ten measurements on each sample; bar graphs show mean and s.d.

Figure 3 | Deep PACT of genetically encoded RS BphP1 *in vivo*. (**a**) PA CNR of BphP1-expressing U87 cells embedded at 10-mm depth versus cell count, quantified from ON-state and differential PA images shown in **Supplementary Figure 4b**. One sample was imaged for each cell count. The data were averaged over ten measurements on each sample and are shown as mean ± s.d. (**b**) *In vivo* whole-body PACT images of the kidney region of a nude mouse, acquired 1 week after injection of ~10^6 BphP1-expressing U87 cells into the left kidney. The ON- and OFF-state PA images clearly show the major blood-enriched internal organs, including the left kidney (LK), right kidney (RK), spinal cord (SC), renal vein (RV), bladder (BL) and spleen (SP). The differential image clearly shows the tumor in the left kidney. Scale bar applies to all images in the panel. (**c**) An overlay of the U87 tumor (in color) in the left kidney and the blood-dominated OFF-state image (in grayscale). Hb, hemoglobin. (**d**) Normalized signal profiles of the ON-state, OFF-state and differential images from the region along the white dashed line in **b**. (**e**) A representative H&E histological image of a harvested left kidney showing the tumor region. (**f**) Deep PACT of a mouse brain U87 tumor expressing BphP1. The tumor (in color) was ~3 mm beneath the scalp surface. A global threshold was applied to all the differential images with a threshold level at three times the noise level.
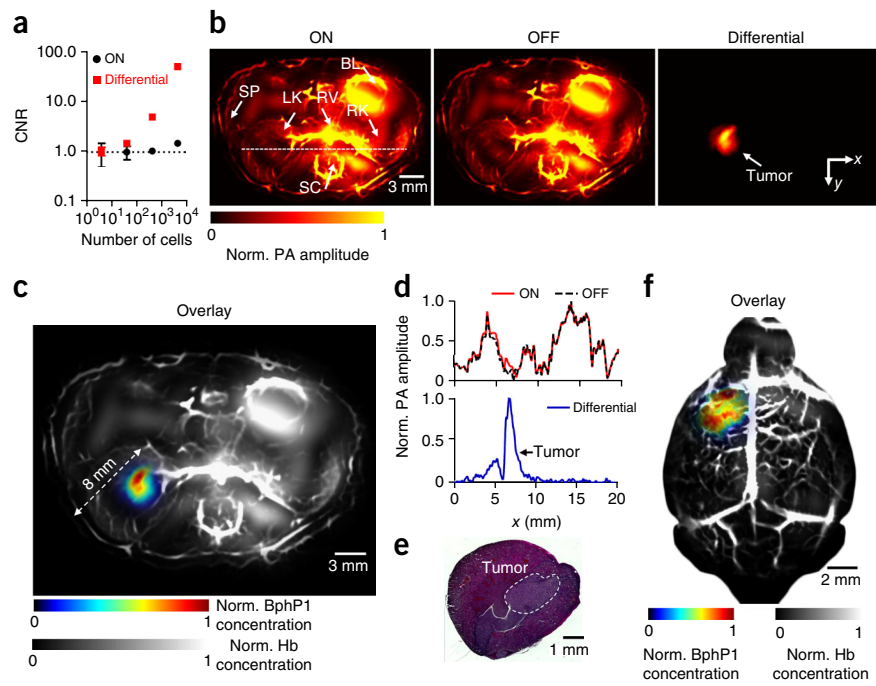
cytometry) during several weeks of continuous cell culturing (**Supplementary Fig. 6b–e**).

To demonstrate RS-PACT *in vivo*, we imaged a mouse 1 week after injection of 10^6 BphP1-expressing U87 cells into the left kidney. We were able to delineate major organs, including the skin, kidneys, spleen, bladder and spinal cord, with strong signals from blood (**Fig. 3b**). The U87 tumor in the left kidney, overwhelmed by the blood signals, could not be detected. By contrast, after 20-cycle photoswitching, the differential PA image clearly showed the tumor at depths up to ~8 mm, with an average CNR of ~20 (**Fig. 3c**). The photoswitchable tumor had different signals in the ON- and OFF-state images, whereas the nonswitchable background signals from blood were virtually identical (**Fig. 3d**). After PA imaging, we confirmed the tumor histologically (**Fig. 3e**). RS-PACT was capable of three-dimensional imaging of a BphP1-expressing tumor (**Supplementary Video 2**). We further demonstrated the superior sensitivity of BphP1-based RS-PACT by comparing the images of a BphP1-expressing U87 tumor and a wild-type U87 tumor (**Supplementary Fig. 7**), and by imaging an otherwise undetectable U87 tumor in a mouse brain at ~3-mm depth beneath the scalp surface (**Fig. 3f** and **Supplementary Fig. 8**).

Longitudinal RS-PACT of tumor metastases
We longitudinally imaged the growth of a BphP1-expressing U87 tumor in a mouse liver and monitored tumor metastases in the liver lobes (*n* = 6) for 1 month (**Fig. 4a**). The differential PA images detected the growth of the primary tumor in the right liver lobe, and later secondary tumors resulted from metastatic spread to other liver lobes (**Fig. 4a**). The smallest secondary tumor had a diameter of ~300 μm. Assuming that the mean diameter of U87 cells is ~10 μm, each resolution voxel of the secondary tumor corresponded to ~3,000 U87 cells. The CNR of the above-mentioned tumor was ~15 in the differential image, which suggests that it is possible to

detect as few as ~200 cells at this depth. Over 1 month, we observed exponential growth of the primary tumor and delayed exponential growth of the secondary tumor (**Fig. 4b**). There was no difference between the growth rates of the primary tumor (from day 0) and the secondary tumors (from day 7). The cross-sectional–area doubling times of the primary tumor and secondary tumors were, respectively, 8.0 ± 1.2 and 7.2 ± 2.7 d, suggesting cell-doubling times of 5.3 ± 0.8 d and 4.8 ± 1.8 d. After the PA imaging, we histologically confirmed the relative locations of the tumors (**Fig. 4c**).

Subdiffraction PAM of BphP1
With tight focusing of the excitation light, PAT can provide optically determined spatial resolution on the scale of micrometers, a technology referred to as optical-resolution PAM[4]. Here we demonstrate that BphP1 improved the image contrast of optical-resolution PAM *in vivo* and, more important, overcame the optical-diffraction limit for super-resolution PA imaging.

We developed a double-illumination PA microscope that illuminates the sample from above and below (**Fig. 5a** and Online Methods). The top illumination utilizes a 0.1–numerical aperture (NA) objective, and the bottom illumination uses a 1.4-NA oil-immersion objective. Because of its relatively large depth of focus (~83 μm), the top illumination is suited for *in vivo* imaging with capillary-level resolution (~3 μm). As a demonstration, we imaged a nude mouse ear bearing BphP1-expressing U87 tumors. The differential image had a ~67-fold greater CNR than the ON-state image (**Supplementary Fig. 9**).

Moreover, we developed subdiffraction PA imaging based on the reversible photoswitching of BphP1 (termed RS-PAM) (**Fig. 5b**, Online Methods and **Supplementary Notes 1–3**). Briefly, when a train of Gaussian-shaped laser pulses at 780 nm repeatedly strike a group of ON-state BphP1 molecules, the PA signals generated by the consecutive laser pulses decrease in amplitude as more and more

Figure 4 | Longitudinal PACT monitoring of cancer metastasis in a mouse liver. (**a**) Whole-body PACT images of the liver region of a representative nude mouse acquired repeatedly for 30 d after the injection of BphP1-expressing U87 cells into the right liver lobe (*n* = 6). Differential signals (in color) are overlaid on top of the structural signals from the blood (in grayscale). The white arrows in the images for day 21 and day 30 indicate secondary tumors due to metastasis. A global threshold was applied to all the differential images with a threshold level at three times the noise level. All the images were first thresholded and then normalized across the measurements. Scale bar applies to all images in the panel. (**b**) Increase in area of primary and secondary tumors. Error bars represent ±s.e.m. for results from six animals. (**c**) Representative H&E histological images of mouse liver lobes with a primary tumor (PT) and secondary tumors (ST). Scale bar applies to both images in the panel.
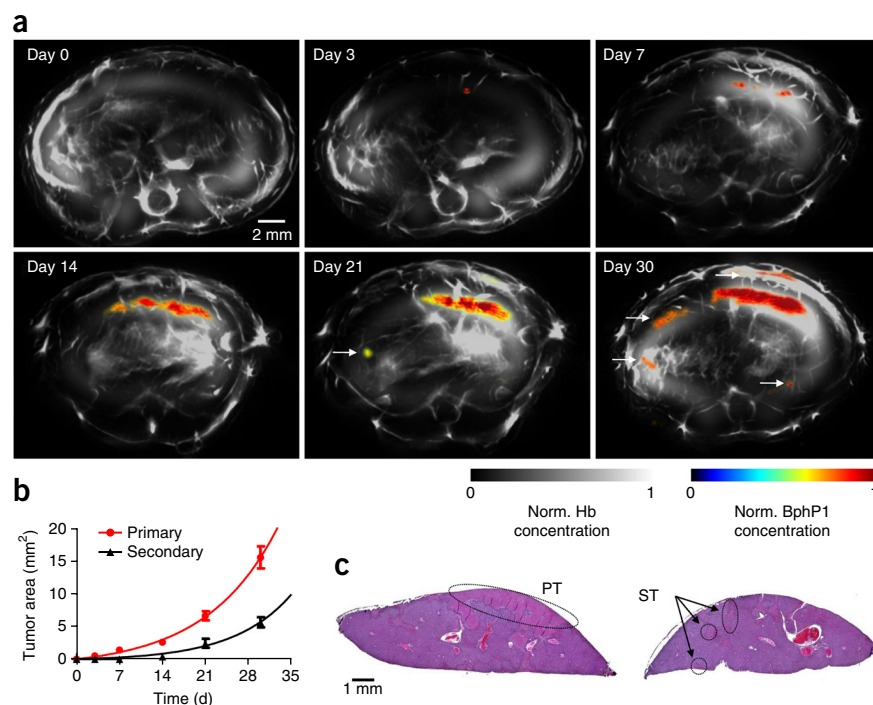

BphP1 molecules are inhomogeneously switched off at a rate proportional to the local excitation intensity (**Supplementary Note 1**). The PA signal from the center of the excitation spot decays faster than that from the periphery. The detected PA-signal decay is integrated over all the molecules in the excitation spot. When a polynomial function is used to fit the signal decay as a function of time, the high-order coefficient of the fitted polynomial imposes nonlinear weighting on the signal contributions from the excitation spot, accentuating the contribution from the center (**Supplementary Note 2**). A higher-order coefficient has a narrower spatial distribution. RS-PAM extracts the highest-order coefficient of the polynomial fitting at each pixel as its image contrast, achieving subdiffraction spatial resolution[29]. Note that the highest-order coefficient that can be effectively

extracted is determined by the signal-to-noise ratio of the original PA-signal decay. By efficiently blocking the out-of-focus signals, RS-PAM provides optical-sectioning capability for laterally large targets (**Supplementary Note 3**), which is not available in conventional PAM[30].

Using the bottom illumination of the PAM system, we demonstrated subdiffraction lateral resolution by imaging a monolayer of BphP1-expressing bacteria densely fixed on a coverslip. At each pixel, we used 100 laser pulses at 780 nm to record the switching-off dynamics of BphP1. We then switched the OFF-state BphP1 molecules back on with 1 s of continuous-wave illumination at 630 nm. Compared with the conventional PAM image, the

Figure 5 | Subdiffraction PAM of RS BphP1 (RS-PAM). (**a**) Schematic of the double-illumination PAM system. BS, beam splitter; DM, dichroic mirror; L1 and L2, laser beams 1 and 2, respectively; M, mirror; OL, optical lens; SOL, silicone oil layer; WT, water tank. Top objective, 0.1 NA; bottom objective, 1.4 NA with oil immersion. (**b**) Principle of RS-PAM with subdiffraction resolution. In the diffraction-limited excitation volume, some ON-state BphP1 molecules (dots) are switched to the OFF state, where the switching-off rate is proportional to the local excitation intensity. By fitting the nonlinear signal-decay dynamics, RS-PAM improves the spatial resolution in all dimensions. (**c**) Conventional (Conv.) PAM and RS-PAM images of BphP1-expressing bacteria densely fixed on a coverslip, showing the superior lateral resolution of RS-PAM. (**d**) Close-up images of the regions enclosed in dashed boxes in **c**. Dashed lines indicate location of signal profiles in **e**. (**e**) Normalized signal profiles across the two bacteria represented in **d**. (**f**) Depth-encoded RS-PAM image of a multiple layer of BphP1-expressing U87 cells fixed on a coverslip. The relative depths of the cells are color-coded from blue (superficial) to red (deep). (**g**) *x-z* cross-sectional images of two stacked U87 cells, acquired with conventional PAM and RS-PAM, showing the substantially finer axial resolution of RS-PAM.
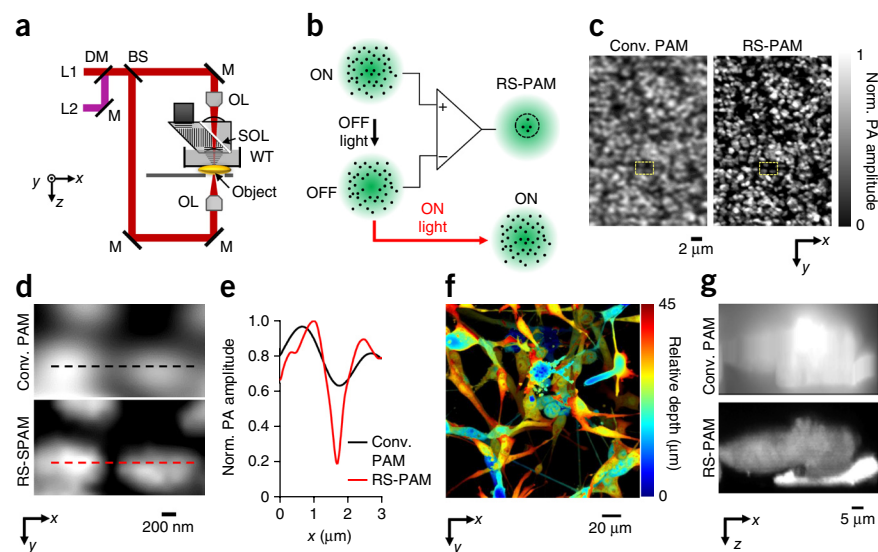
RS-PAM image showed superior lateral resolution, enabling better separation of neighboring bacteria (**Fig. 5c–e**). RS-PAM achieved a lateral resolution of ~141 nm, approximately twofold finer than that of conventional PAM (**Supplementary Fig. 10a**).

We demonstrated the axial resolution of RS-PAM on a multilayer of fixed BphP1-expressing U87 cells (total thickness, ~35 μm). For laterally large targets, conventional PAM exhibited poor axial resolution (~30 μm) as a result of the time-resolved acoustic detection (**Supplementary Fig. 10b**), and therefore was not able to resolve different layers of U87 cells (**Supplementary Fig. 11**). In comparison, RS-PAM was able to block the PA signals generated by the out-of-focus cells and consequently achieved thin optical sectioning of ~0.4 μm, ~75-fold finer than that of conventional PAM (**Supplementary Fig. 10b**). By depth scanning, RS-PAM clearly resolved U87 cells at different layers (**Fig. 5f,g**, **Supplementary Fig. 11** and **Supplementary Video 3**).

DISCUSSION

We have developed PAT that—for the first time, to our knowledge—combines deep-tissue PA imaging with a reversibly switchable, nonfluorescent, photochromic, NIR bacterial phytochrome, BphP1. With this new imaging technology, we achieved PA detection sensitivity of tens to hundreds of live mammalian cells at 1-cm depth. Moreover, with PA imaging of BphP1, we achieved enhanced image contrast of optical-resolution PAM *in vivo* and subdiffraction imaging of individual cells.

These achievements are the result of BphP1's unique photochemical features. First, BphP1 has two red- and NIR-absorbing photoconvertible states, enabling deep-tissue PA imaging and photoswitching[20]. Second, BphP1 is noncytotoxic and does not affect cell metabolism. Third, BphP1 efficiently and specifically binds the endogenous chromophore BV and does not require an exogenous supply; mammalian cells in different organs generally have sufficient BV for BphP1 binding. Fourth, BphP1 exhibits low photoswitching fatigue during photoconversion, allowing for longitudinal imaging.

PAT is inherently suited to take maximum advantage of BphP1's photochemical features. First, PAT can provide high-resolution imaging of BphP1 at depths beyond those achieved by pure optical techniques[26]. Second, in comparison to traditional multiwavelength methods[31], single-wavelength imaging at 780 nm greatly reduces the influence of unknown local light fluence (in joules per square centimeter) on extraction of the protein signals. The wavelength-dependent local light fluence is affected by not only the optical attenuation of the intervening tissue but also the local optical absorption[31,32]. Third, because of the relatively low light attenuation in the red and NIR regions, the switching efficiency of BphP1 can be maintained in deep tissue. Finally, the differential imaging process is simple and reliable. The background signals are removed without a loss of either spatial resolution or sensitivity[12,31].

We carefully mitigated potential artifacts in our differential images. First, BphP1-expressing cells had relatively weak absorption. The photoswitching of the cells had negligible influence on the total internal optical fluence distribution. Second, for *in vivo* imaging, animal motion was largely minimized by our specially designed animal-mounting methods (Online Methods). Image averaging over multiple switching cycles further decreased motion artifacts. Third, the fluctuation in laser-pulse energy was less than 3%, and its effect was further minimized by multiplexed data

acquisition and multicycle averaging. Finally, signal thresholding removed remaining artifacts.

Further development of the technology could include improvement of the NIR photochromic probes, either by engineering BphP1 properties[16] or by seeking better BphPs in nature[18]. Relatively inexpensive continuous-wave laser diodes can be used for photoswitching[33]. The current PACT has a relatively low imaging speed (32 s per switching cycle and 11 min with 20 averaging cycles). The imaging speed can be improved with the use of a 50-Hz laser and a 512-channel data-acquisition system, which can avoid the data multiplexing and thus reduce the imaging time.

Overall, BphP1-based PAT introduces new possibilities for biomedical applications. For example, transgenic mouse models that express BphP1 in neurons can be used for longitudinal PA monitoring of neural network development[34]. BphP1-expressing cardiomyocytes should allow direct PA imaging of heart activity, which is otherwise challenging because of the large amount of blood inside the heart. The high detection sensitivity of BphP1 will be useful for capturing nonpigmented cancer cells circulating in the blood in deep tissue[35], as well as for cell tracking in immunotherapy[36].

METHODS

Methods and any associated references are available in the online version of the paper.

Note: Any Supplementary Information and Source Data files are available in the online version of the paper.

AUTHOR CONTRIBUTIONS

J.Y., V.V.V. and L.V.W. conceived and designed the study. J.Y., L.L. and L.W. constructed the imaging system. A.A.K. and D.M.S constructed the plasmids, purified and characterized the proteins *in vitro*, and established the stable bacterial and mammalian cell clones. J.Y., L.L., G.L. and R.Z. performed photoacoustic experiments and analyzed the data. V.V.V. and L.V.W. supervised the study. All authors wrote the manuscript.

1. Ntziachristos, V. Going deeper than microscopy: the optical imaging frontier in biology. *Nat. Methods* **7**, 603–614 (2010).
2. Weissleder, R. & Pittet, M.J. Imaging in the era of molecular oncology. *Nature* **452**, 580–589 (2008).
3. Rice, W.L., Shcherbakova, D.M., Verkhusha, V.V. & Kumar, A.T.N. *In vivo* tomographic imaging of deep-seated cancer using fluorescence lifetime contrast. *Cancer Res.* **75**, 1236–1243 (2015).
4. Wang, L.V. & Hu, S. Photoacoustic tomography: *in vivo* imaging from organelles to organs. *Science* **335**, 1458–1462 (2012).
5. Brecht, H.P. *et al.* Whole-body three-dimensional optoacoustic tomography system for small animals. *J. Biomed. Opt.* **14**, 064007 (2009).
6. Kruger, R.A., Lam, R.B., Reinecke, D.R., Del Rio, S.P. & Doyle, R.P. Photoacoustic angiography of the breast. *Med. Phys.* **37**, 6096–6100 (2010).

7. de la Zerda, A., Kim, J.W., Galanzha, E.I., Gambhir, S.S. & Zharov, V.P. Advanced contrast nanoagents for photoacoustic molecular imaging, cytometry, blood test and photothermal theranostics. *Contrast Media Mol. Imaging* **6**, 346–369 (2011).

8. Luke, G.P., Yeager, D. & Emelianov, S.Y. Biomedical applications of photoacoustic imaging with exogenous contrast agents. *Ann. Biomed. Eng.* **40**, 422–437 (2012).

9. Kircher, M.F. *et al.* A brain tumor molecular imaging strategy using a new triple-modality MRI-photoacoustic-Raman nanoparticle. *Nat. Med.* **18**, 829–834 (2012).

10. Wang, X. *et al.* Noninvasive laser-induced photoacoustic tomography for structural and functional *in vivo* imaging of the brain. *Nat. Biotechnol.* **21**, 803–806 (2003).

11. Zhang, H.F., Maslov, K., Stoica, G. & Wang, L.H.V. Functional photoacoustic microscopy for high-resolution and noninvasive *in vivo* imaging. *Nat. Biotechnol.* **24**, 848–851 (2006).

12. Razansky, D. *et al.* Multispectral opto-acoustic tomography of deep-seated fluorescent proteins *in vivo*. *Nat. Photonics* **3**, 412–417 (2009).

13. Krumholz, A., Shcherbakova, D.M., Xia, J., Wang, L.V. & Verkhusha, V.V. Multicontrast photoacoustic *in vivo* imaging using near-infrared fluorescent proteins. *Sci. Rep.* **4**, 3939 (2014).

14. Stiel, A.C. *et al.* High-contrast imaging of reversibly switchable fluorescent proteins via temporally unmixed multispectral optoacoustic tomography. *Opt. Lett.* **40**, 367–370 (2015).

15. Jathoul, A.P. *et al.* Deep *in vivo* photoacoustic imaging of mammalian tissues using a tyrosinase-based genetic reporter. *Nat. Photonics* **9**, 239–246 (2015).

16. Piatkevich, K.D., Subach, F.V. & Verkhusha, V.V. Engineering of bacterial phytochromes for near-infrared imaging, sensing, and light-control in mammals. *Chem. Soc. Rev.* **42**, 3441–3452 (2013).

17. Weissleder, R. & Ntziachristos, V. Shedding light onto live molecular targets. *Nat. Med.* **9**, 123–128 (2003).

18. Giraud, E. & Vermeglio, A. Bacteriophytochromes in anoxygenic photosynthetic bacteria. *Photosynth. Res.* **97**, 141–153 (2008).

19. Auldridge, M.E. & Forest, K.T. Bacterial phytochromes: more than meets the light. *Crit. Rev. Biochem. Mol. Biol.* **46**, 67–88 (2011).

20. Shcherbakova, D.M. & Verkhusha, V.V. Near-infrared fluorescent proteins for multicolor *in vivo* imaging. *Nat. Methods* **10**, 751–754 (2013).

21. Subach, F.V. *et al.* Red fluorescent protein with reversibly photoswitchable absorbance for photochromic FRET. *Chem. Biol.* **17**, 745–755 (2010).

22. Pletnev, S., Subach, F.V., Dauter, Z., Wlodawer, A. & Verkhusha, V.V. A structural basis for reversible photoswitching of absorbance spectra in red fluorescent protein rsTagRFP. *J. Mol. Biol.* **417**, 144–151 (2012).

23. Xia, J. *et al.* Whole-body ring-shaped confocal photoacoustic computed tomography of small animals *in vivo*. *J. Biomed. Opt.* **17**, 050506 (2012).

24. Lai, P., Xu, X. & Wang, L.V. Dependence of optical scattering from Intralipid in gelatin-gel based tissue-mimicking phantoms on mixing temperature and time. *J. Biomed. Opt.* **19**, 35002 (2014).

25. Piatkevich, K.D., Subach, F.V. & Verkhusha, V.V. Far-red light photoactivatable near-infrared fluorescent proteins engineered from a bacterial phytochrome. *Nat. Commun.* **4**, 2153 (2013).

26. Yan, Y., Marriott, M.E., Petchprayoon, C. & Marriott, G. Optical switch probes and optical lock-in detection (OLID) imaging microscopy: high-contrast fluorescence imaging within living systems. *Biochem. J.* **433**, 411–422 (2011).

27. Toh, K.C., Stojkovic, E.A., van Stokkum, I.H., Moffat, K. & Kennis, J.T. Proton-transfer and hydrogen-bond interactions determine fluorescence quantum yield and photochemical efficiency of bacteriophytochrome. *Proc. Natl. Acad. Sci. USA* **107**, 9170–9175 (2010).

28. Habuchi, S. *et al.* Reversible single-molecule photoswitching in the GFP-like fluorescent protein Dronpa. *Proc. Natl. Acad. Sci. USA* **102**, 9511–9516 (2005).

29. Yao, J. *et al.* Reversibly switchable fluorescence microscopy with enhanced resolution and image contrast. *J. Biomed. Opt.* **19**, 086018 (2014).

30. Yao, J., Wang, L., Li, C., Zhang, C. & Wang, L.V. Photoimprint photoacoustic microscopy for three-dimensional label-free subdiffraction imaging. *Phys. Rev. Lett.* **112**, 014302 (2014).

31. Deliolanis, N.C. *et al.* Deep-tissue reporter-gene imaging with fluorescence and optoacoustic tomography: a performance overview. *Mol. Imaging Biol.* **16**, 652–660 (2014).

32. Ntziachristos, V. & Razansky, D. Molecular imaging by means of multispectral optoacoustic tomography (MSOT). *Chem. Rev.* **110**, 2783–2794 (2010).

33. Xia, J. & Wang, L.V. Small-animal whole-body photoacoustic tomography: a review. *IEEE Trans. Biomed. Eng.* **61**, 1380–1389 (2014).

34. Devor, A. *et al.* The challenge of connecting the dots in the BRAIN. *Neuron* **80**, 270–274 (2013).

35. Chaffer, C.L. & Weinberg, R.A. A perspective on cancer cell metastasis. *Science* **331**, 1559–1564 (2011).

36. Couzin-Frankel, J. Cancer immunotherapy. *Science* **342**, 1432–1433 (2013).

ONLINE METHODS

PAT. In PAT, as photons propagate in tissue, some are absorbed by biomolecules, and their energy is partially or completely converted into heat. The heat-induced pressure propagates in tissue and is detected outside the tissue by an ultrasonic transducer or transducer array to form an image that maps the original optical energy deposition in the tissue. Depending on the image-formation method used, PAT has two major implementations. The first, direct image formation, is based on mechanical scanning of a focused single-element ultrasonic transducer and is commonly used in PAM. The second, reconstruction image formation, is based on parallel detection by an unfocused multi-element ultrasonic transducer array or a mechanical or electronic scanning equivalent and is used in PACT.

Plasmid construction and protein expression. The *Rp*BphP1 gene was kindly provided by E. Giraud (Institute for Research and Development). For mammalian expression, the BphP1 gene was PCR amplified as *Nhe*I-BglII fragments and cloned into multicloning sites of the pIRES2-EGFP vector (Takara-Clontech), which allowed for coexpression of BphP1 and EGFP proteins separately but from the same bicistronic mRNA. For bacterial expression of BphP1, we used the pBAD/His-B vector (Life Technologies).

rsTagRFP and iRFP720 were purified from *Escherichia coli* as described[20,21]. BphP1 with a polyhistidine tag at the N terminus was expressed in LMG194 bacterial cells (Life Technologies) containing a pWA23h plasmid encoding heme oxygenase for BV synthesis in *E. coli*[20,25]. We grew the bacterial cells in RM medium supplemented with ampicillin, kanamycin and 0.02% rhamnose for 6–8 h and then induced protein expression by adding 0.002% arabinose. We purified the proteins using nickel–nitrilotriacetic acid agarose (Qiagen).

Absorption spectra of BphP1 dissolved in phosphate-buffered saline were measured using a standard spectrophotometer (Hitachi U-2000) with a 100-µL quartz microcuvette (Starna Cells). The spectrum of the ON-state BphP1 was measured without a photoswitching light source, because the ON state was the ground state (or natural state). To measure the OFF-state spectra, we carried out photoswitching with a 780/25-nm LED placed above the microcuvette. The photoswitching beam direction was orthogonal to the optical beam path of the spectrophotometer. The OFF-state spectra were measured after the photoswitching was completed and the LED was turned off, so there was no interference with the measurements. Because of the extremely low light intensity ($<1\,\mu W/cm^2$), changes in the absorption spectra of BphP1 induced by the light illumination inside the spectrophotometer were negligible.

The photoswitching of BphP1 shown in **Figure 2a** was accomplished with 780/25-nm and 630/25-nm LEDs, which were mounted orthogonally to the optical beam path of the spectrophotometer to avoid detection interference. BphP1 was photoswitched directly in the 100-µL quartz microcuvette of the spectrophotometer while its absorbance at 780 nm was measured.

Mammalian cell culture. U87 cells were grown in DMEM supplemented with 10% FBS, penicillin-streptomycin mixture and 2 mM glutamine (all from Life Technologies) at 37 °C in 5% CO_2 air atmosphere. We obtained a U87 stable preclonal mixture by transfecting cells with pBphP1-IRES2-EGFP plasmid. Plasmid transfection was performed using an Effectene reagent (Qiagen).

Cells were further selected with 700 µg/ml of G418 antibiotic for 2 weeks and enriched using a FACSAria sorter (BD Biosciences) equipped with a 488-nm laser and a 530/30-nm emission filter. For further culturing of U87 cells stably expressing BphP1, the medium was additionally supplemented with 500 µg/ml of G418 (Corning). To implant xenograph tumors into animals (brain, kidney or liver), we injected about 10^6 U87 cells, either stably expressing BphP1 or unmodified, in 0.2 mL of PBS into mice with the guidance of a commercial ultrasound system (Vevo LAZR, Visualsonics). For photoacoustic microscopy with subdiffraction resolution, we plated U87 cells in a 35-mm glass-bottom petri dish (P35GCOL-0-14-C, MatTek).

We measured the expression level of EGFP during prolonged culturing of a BphP1-expressing U87 preclonal cell mixture using an LSRII flow cytometer (BD Biosciences) equipped with a 488-nm laser and a 530/40-nm emission filter. For cell-viability assay, wild-type U87 cells and BphP1-expressing U87 cells were stained with annexin V conjugated with allophycocyanin dye according to the manufacturer's protocol (BD Biosciences). We analyzed cells with the LSRII flow cytometer equipped with a 640-nm laser and 660/20-nm emission filter. We estimated the cell viability on the basis of the percentage of annexin V–negative cells. Typically, the cell samples were triplicated, and at least 10^4 cells were analyzed per sample.

Animal preparation. Adult, 2–3-month-old female nude mice (Hsd:Athymic Nude-Foxl[NU], Harlan Co.; body weight, ~20–30 g) were used for all *in vivo* experiments. All experimental procedures were carried out in conformity with laboratory animal protocols approved by the Animal Studies Committee at the Washington University in St. Louis. Throughout the experiment, the mouse was maintained under anesthesia with 1.5% vaporized isoflurane. The mouse was taped to a lab-made motorized animal holder, which held the animal upright during imaging. The top of the holder was a small aluminum tube affixed to the animal's nose and mouth, and the bottom was an aluminum cylinder attached to a permanent magnet. The magnet securely held the animal holder to the scanning stage for elevational scanning. The animal's fore and hind legs were taped to the top and bottom parts of the holder, respectively. The two parts were connected by four lengths of high-strength fishing line (0.13-mm diameter braided line). The combination of the magnet and a counterweight kept the thin lines in tension to minimize holder movement caused by animal respiratory motion[23]. The animal's trunk was immersed in water, and its body temperature was maintained at 37 °C by the water, which circulated through a heating bath outside the tank.

Hematoxylin and eosin (H&E) histology and fluorescence imaging. Tumor-bearing kidneys and livers were harvested and fixed in 4% paraformaldehyde for 24 h. Coronal sections (5 µm thick) were cut with paraffin embedding. Standard H&E staining was performed on the sections, which were examined using bright-field microscopy (NanoZoomer, Hamamatsu) with a 20×/0.67-NA objective.

The harvested tissue and the BphP1-expressing U87 cells were also imaged by wide-field fluorescence microscopy (Fluoview 1000, Olympus) using the coexpressed EGFP (excitation wavelength, 488 nm; emission filter wavelength, 510 nm). A 4×/0.10-NA objective was used to image the harvested tissue, and a 20×/0.70-NA objective was used to image the cells.

Whole-body PACT of RS phytochrome BphP1 (RS-PACT). The whole-body PACT system used in this study was upgraded from our previous work[23] (**Fig. 1b**). To image BphP1 and other control proteins, we combined a Ti:sapphire laser (LS-2137/LT-2211A, LOTIS) and a lab-made optical parametric oscillator laser, each pumped by an Nd:YAG laser with a 10-Hz pulse-repetition rate. The 780-nm light from the Ti:sapphire laser was used for both whole-body PA imaging and switching off of BphP1 at the same time, and the 630-nm light from the optical parametric oscillator laser was used to switch on the protein. The flashlamps of the two pump lasers are synchronized, and the two lasers are individually triggered by a field-programmable-gate-array–based controller (sbRIO9323, National Instruments). The two laser beams are combined by a dichroic mirror, and their incident fluences (in millijoules per square centimeter) are measured by an optical power meter. The laser beam is first homogenized by an optical diffuser (EDC-5, RPC Photonics) and then passed through a conical lens (cone angle, 130°; Delmar Photonics) to form a ring-shaped light pattern. The light is then passed through an optical condenser to form a ring-shaped light band around the animal's trunk. The light incident area is aligned slightly above the acoustic focal plane to ensure sufficient light diffusion. The thickness of the light band is ~5 mm, and its diameter is similar to the cross-sectional diameter of a mouse (~2–3 cm). The maximum light fluence on the skin of the animal is ~8 mJ/cm^2, which is well below the American National Standards Institute safety limit.

The PA signals are detected by a full-ring ultrasonic transducer array (Imasonic) with a 5-cm diameter, a 5-MHz central frequency, more than 80% one-way bandwidth, and 512 elements. Each element (10-mm height, 0.3-mm pitch and 0.1-mm inter-element space) is cylindrically focused to produce an axial focal distance of 19.8 mm (acoustic NA, 0.25). The combined foci of all 512 elements form an approximately uniform imaging region with a 20-mm diameter and 1-mm thickness. In this region, the radial resolution is 100 µm, and the tangential resolution is 100–250 µm, where the tangential direction is perpendicular to the radial direction. The tangential resolution depends on the radial distance from the center and degrades slowly with the radial distance. The data-acquisition system has 64 channels with eightfold multiplexing. The cross-sectional imaging speed is 1.6 s per frame. For image reconstruction, the raw data from each element are first Wiener deconvolved to account for the ultrasonic transducer's impulse response and then reconstructed in each imaging plane, on the basis of the universal back-projection algorithm[37]. To mitigate the artifacts induced by acoustic heterogeneities in the animal body, such as air cavities in the gastrointestinal tract and backbone, the half-time image-reconstruction algorithm is applied in combination with the universal back-projection reconstruction[38].

Subdiffraction PAM of RS phytochrome BphP1 (RS-PAM). As shown in **Figure 5a**, a pulsed Nd:YLF laser (Innoslab, 523 nm, Edgewave) pumps a dye laser (CBR-D, Sirah) to provide 780-nm light for PA imaging and switching off of BphP1. A continuous-wave 630-nm laser diode (Information Unlimited) switches on the protein. The light beams are combined by a dichroic mirror, reshaped by an iris (ID25SS, Thorlabs) and attenuated by a neutral density filter (NDC-50C-2M, Thorlabs). The attenuated beam is then split into two sub-beams (top and bottom) by a 50-50 beam splitter (BSW04, Thorlabs). The top beam is focused by a condenser lens (LA1131, Thorlabs) before passing through a 50-µm pinhole (P50C, Thorlabs) for further spatial filtering. The filtered beam is then focused by an optical objective (AC127-050-A, Thorlabs; NA, 0.1 in air) into the object from the top. A beam combiner composed of a thin layer of silicone oil sandwiched between a right-angle prism (NT32-545, Edmund Optics) and a rhomboid prism (NT49-419, Edmund Optics) provides acoustic-optical coaxial alignment. The resultant PA waves are detected by an ultrasonic transducer (V214-BB-RM, Olympus-NDT) with a central frequency of 50 MHz. An acoustic lens with a 0.5 NA is ground into the bottom of the rhomboid prism to provide an acoustic focal diameter of 30 µm. An optical correction lens is attached to the top of the beam combiner to correct aberration. The acoustic lens is submerged in a water tank for ultrasound coupling. The bottom beam duplicates the path of the top beam, except that it is directly focused into the object from the bottom without going through the beam combiner and water tank. The bottom objective has a 1.4 NA with oil immersion (MPLAPON100XO, Olympus). By carefully adjusting the positions of the two objectives, we were able to achieve a confocal configuration of the two optical foci and the acoustic focus. Volumetric imaging is acquired by means of two-dimensional raster scanning of the object. A photodiode is added to monitor the fluctuations of the laser-pulse energy.

The mechanism of the lateral-resolution enhancement of RS-PAM is illustrated in **Figure 5b**. The mathematical details are elaborated in **Supplementary Notes 1–3**. The effective lateral point-spread function of the system is $(0.51/\sqrt{1+bm}) \times (\lambda_0/NA)$, where b is the power dependence of the switching-off rate on the excitation intensity ($b = 1$ for BphP1), m is the order of polynomial fitting of the signal decay ($m = 3$ in this study), λ_0 is the excitation wavelength, and NA is the numerical aperture of the objective[29]. The lateral resolution of RS-PAM is finer than that of conventional PAM by a factor of $\sqrt{1+bm}$.

In addition to the subdiffraction lateral resolution, the nonlinear nature of the RS-PAM signal enables optical sectioning in the axial direction, which is of particular interest for large (or planar) targets. Compared with the in-focus molecules, the out-of-focus molecules are less affected during the switching-off process. Therefore, high-order coefficients extracted from the polynomial fitting of the signal decay contain mainly in-focus contributions, and thus RS-PAM achieves optical sectioning. Like the lateral-resolution enhancement, the optical-sectioning strength of RS-PAM is determined by the power dependence of the switching-off rate on the excitation intensity. For point targets, RS-PAM can achieve an axial resolution of $1.8\sqrt{2^{1/(1+bm)}-1} \times (\lambda_0/NA^2)$ (ref. 30). For large targets, RS-PAM can achieve an axial resolution of $1.8\sqrt{2^{1/bm}-1} \times (\lambda_0/NA^2)$.

Reproducibility. The experiments were not randomized. The investigators were not blinded to allocation during experiments and outcome assessment. No sample-size estimation was performed to ensure adequate power to detect a prespecified effect size.

37. Xu, M. & Wang, L.V. Universal back-projection algorithm for photoacoustic computed tomography. *Phys. Rev. E* **71**, 016706 (2005).
38. Anastasio, M.A. *et al.* Half-time image reconstruction in thermoacoustic tomography. *IEEE Trans. Med. Imaging* **24**, 199–210 (2005).